

Experimental demonstration of continuous quantum error correction

William P. Livingston,^{1,2} Machiel S. Blok,^{1,2,3} Emmanuel Flurin,⁴

Justin Dressel,^{5,6} Andrew N. Jordan,^{3,5} and Irfan Siddiqi^{1,2}

¹*Department of Physics, University of California, Berkeley, CA 94720 USA*

²*Center for Quantum Coherent Science, University of California, Berkeley, California 94720, USA**

³*Department of Physics and Astronomy, University of Rochester, Rochester, New York 14627, USA*

⁴*Université Paris-Saclay, CEA, CNRS, SPEC, 91191 Gif-sur-Yvette Cedex, France*

⁵*Institute for Quantum Studies, Chapman University, Orange, CA 92866, USA*

⁶*Schmid College of Science and Technology, Chapman University, Orange, CA 92866, USA*

(Dated: July 27, 2021)

The storage and processing of quantum information are susceptible to external noise, resulting in computational errors that are inherently continuous[1]. A powerful method to suppress these effects is to use quantum error correction[2–4]. Typically, quantum error correction is executed in discrete rounds where errors are digitized and detected by projective multi-qubit parity measurements[5, 6]. These stabilizer measurements are traditionally realized with entangling gates and projective measurement on ancillary qubits to complete a round of error correction. However, their gate structure makes them vulnerable to errors occurring at specific times in the code and errors on the ancilla qubits. Here we use direct parity measurements to implement a continuous quantum bit-flip correction code in a resource-efficient manner, eliminating entangling gates, ancilla qubits, and their associated errors. The continuous measurements are monitored by an FPGA controller that actively corrects errors as they are detected. Using this method, we achieve an average bit-flip detection efficiency of up to 91%. Furthermore, we use the protocol to increase the relaxation time of the protected logical qubit by a factor of 2.7 over the relaxation times of the bare comprising qubits. Our results showcase resource-efficient stabilizer measurements in a multi-qubit architecture and demonstrate how continuous error correction codes can address challenges in realizing a fault-tolerant system.

A successful quantum error correction (QEC) code decreases logical errors by redundantly encoding information and detecting errors in a more complex physical system. Such a system includes both the qubits encoding the logical quantum information and the overhead resources to perform stabilizer measurements. In a fault-tolerant QEC code, the benefit from error correction needs to outweigh the cost of extra errors associated with this overhead. In the past decade, discrete QEC has been realized in various physical systems such as ion traps[7–9], defects in diamonds[10], and superconducting circuits[11–17]. The stabilizer measurements in these realizations are a dominant source of error [17] because they are indirect and require extra resources, including ancillas and entangling gates.

We demonstrate an alternative form of QEC known as continuous QEC in which continuous stabilizer measurements eliminate the cycles of discrete error correction as well as the need for ancilla qubits and entangling gates[18–20]. Continuous measurements have previously been used to study the dynamics of wavefunction collapse and, with the addition of classical feedback, to stabilize qubit trajectories and correct for errors in single qubit dynamics[21–23]. In systems of two or more qubits, direct measurements of parity can be used to prepare entangled states through measurement[24–29]. Here, we

use two direct continuous parity measurements and associated filtering[30] to correct bit-flip errors while maintaining logical coherence. Errors are detected on a rolling basis, with the measurement rate as the primary limitation to how quickly errors are detected.

We realize our code in a planar superconducting architecture using three transmons as the bare qubits. As depicted in Fig. 1, we implement the ZZ parity measurements using two pairs of qubits coupled to joint readout resonators[29, 31]. Each resonator is coupled to its associated qubits with the same dispersive coupling χ_i with i indexing the resonator, thereby making the resonator reflection response when the associated qubit pair is in $|01\rangle$ identical to the response when the pair is in $|10\rangle$. For each resonator, we set the parity probe frequency to be at the center of this shared odd parity resonance. To approximately implement a full parity measurement, we make the line-width κ_i (636 kHz, 810 kHz) of each resonator smaller than its respective dispersive shift χ_i (2.02 MHz, 2.34 MHz). When the qubit pair is in either $|00\rangle$ or $|11\rangle$, the resonance frequency is sufficiently detuned from the odd parity probe tone to keep the cavity population low and the reflected phase responses for the two even states nearly identical. After reflecting a parity tone off a cavity, the signal is amplified by a Josephson Parametric Amplifier[32] in phase-sensitive mode aligned with the informational quadrature.

We implement the three qubit repetition code using two ZZ parity measurements as stabilizers: Z_0Z_1 and Z_1Z_2 , with Z_j being the Pauli Z operator on qubit

* Correspondence and requests for materials should be addressed to W.P.L. (email: wlivingston@berkeley.edu).

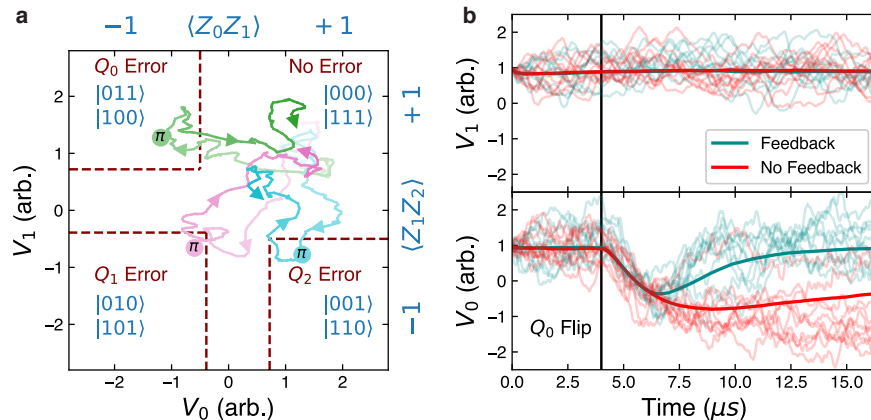


FIG. 2. Error Correction. **a**, Sample experimental voltage traces of the controller correcting induced bit flips. With no errors, both voltages remain positive. When an error occurs, one or both of the voltages flip and the cross thresholds, triggering the controller to send a corrective π pulse to bring the system back to the codespace. **b**, Voltage responses to an induced flip on Q_0 with (blue) and without (red) feedback. Bold lines are averages and light lines are sample individual traces.

steady state, we apply a π -pulse to one of the qubits, inducing a controlled error. We record if and when the controller detects the error and sends out a correction pulse. Errors are successfully detected on Q_0 with 90% efficiency, Q_1 with 86% efficiency, and Q_2 with 91% efficiency. The primary source of inefficiency is T_1 decay bringing the qubits back to ground before detection can happen. On average, the controller corrects an error 3.1-3.4 μs after the error occurs, with the full probability density function over time shown in Fig. 3a. We also characterize a dark count rate for each flip variety by measuring the rate at which the controller detects a qubit flip after preparing in the ground state (3.4, 1.0, 4.0) ms^{-1} . In comparison, the thermal excitation rates for each qubit are estimated to be (1.8, 1.0, 2.0) ms^{-1} .

We next investigate the dominant source of logical errors while running the code: two bit flips occurring in quick succession. When two different qubits flip close together in time relative to the inverse measurement rate, the controller may incorrectly interpret the signals as an error having occurred on the unflipped qubit. The controller then flips this remaining qubit, resulting in a logical error. For continuous error correction, this effect results in a time after an error occurs we call the dead time, when a following error cannot be reliably corrected. To characterize this behavior, we prepare the system in the ground state and apply two successive bit-flips with different times between the pulses. We then check if the controller responds with the right sequence of correction pulses. In Fig. 3b, we show the controller's interpretation of successive flips on Q_0 and Q_2 as a function of time between them. We mark the dead time at the point where the probability of a logical error crosses the probability of successfully correcting the state. Among the possible pairs and orderings of two qubit errors, the dead times vary from 1.6-2.6 μs .

Although the code is designed to correct bit-flip errors, the code will also protect the logical computational basis states against qubit decay, extending the T_1 lifetimes of the logical system beyond that of the bare qubits. As opposed to a bit-flip, a qubit decaying loses any coherent phase of the logical state, and the system will be corrected to a mixed state with the same probability distribution in the computational basis as the initial state. For example, the state $\frac{1}{\sqrt{2}}(|0_L\rangle + |1_L\rangle)$ undergoing a qubit decay and correction will be restored as the density matrix $\frac{1}{2}(|0_L\rangle\langle 0_L| + |1_L\rangle\langle 1_L|)$. In the long time limit of active feedback, the system will reach a steady state described by a mixed density matrix with the majority of population (87-99.6%) in the selected codespace. The T_1 of a codespace is defined by the exponential time constant at which population of computational basis states in the codespace approach this steady state. The different codespaces of different parities have different T_1 decay times, with the longest decay time of 66 μs associated with the odd-odd subspace, as shown in Fig. 3c. The shortest lifetime, 32 μs , is associated with the even-even subspace, since the higher energy level in this codespace has three bare excitations and the lower energy has no excitations. In comparison, the bare T_1 values of the bare qubits range from 20-24 μs , making the logical qubit excited life 2.7 times longer than that of a bare qubit.

Although phase errors are not protected against by this code, an ideal implementation of a bit-flip code should not increase their occurrence rate. However, with our physical realization of continuous correction, we induce extra dephasing in the logical subspace through three primary channels: continuous dephasing due to the measurement tone; dephasing when going from an odd parity subspace to an even parity subspace; and dephasing related to static ZZ interactions intrinsic to the chip design.

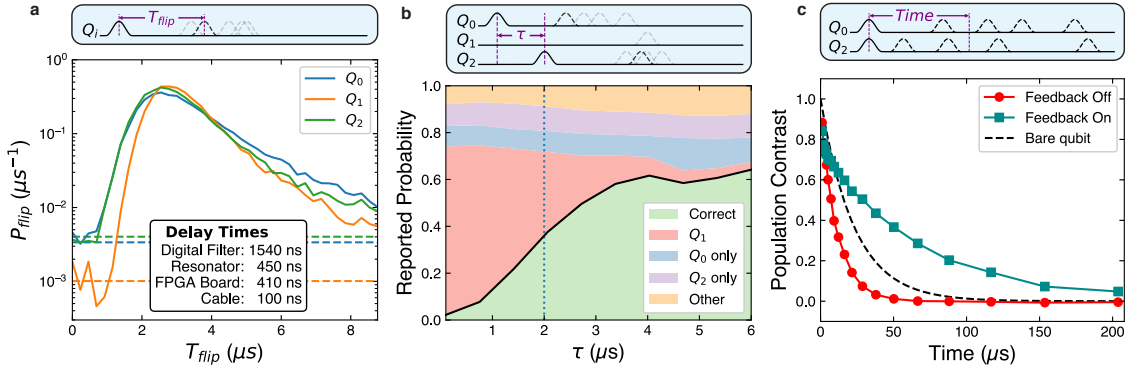


FIG. 3. Characterizing the time to correct an error. **a**, Histogram of time between an induced error and the correction pulse for each of the qubits, normalized such the integral of the probability density $P_{flip}(t)$ gives the detection probability. Dashed lines indicate the dark count rates for each error type. **b**, Probability of detecting certain flip sequences given a flip on Q_0 preceding a flip on Q_2 . The green region is the probability of the controller correctly detecting a Q_0 flip and then a Q_2 flip. The red region is the probability of the controller detecting a Q_1 flip, resulting in a logical error. The dotted line indicates the dead time, when these two probabilities are equal. **c**, Population decay of the excited logical state, $|101\rangle$, of the odd-odd subspace with and without feedback. With feedback on, the lifetime of the logical basis state is longer than that of an individual bare qubit.

The first source of excess dephasing is measurement-induced dephasing, where the dephasing rate is proportional to the distinguishability of different qubit eigenstates under the measurement[37]. Distinguishability is measured as $D_{m,n}^{(i)} = |\alpha_{|m\rangle}^{(i)} - \alpha_{|n\rangle}^{(i)}|^2$ where $|m\rangle$ and $|n\rangle$ are different basis states of the two qubits coupled to resonator i , and $\alpha^{(i)}$ is the resonator's associated coherent state[37]. By tuning the qubit frequencies, the dispersive shifts of the system are calibrated such that $D_{01,10}^{(i)}$ are close to zero. The parity measurement distinguishability ($D_{01,11}^{(i)} \approx D_{01,00}^{(i)}$) determines the measurement-induced dephasing rate of the code. Due to finite χ/κ , the even subspaces are not perfectly indistinguishable, with the theoretical distinguishability ratio $D_{00,01}^{(i)}/D_{00,11}^{(i)} \approx 4(\chi_i/\kappa_i)^2$. We use this formula to calculate distinguishability ratios of 40 and 33 for resonator 0 and 1 respectively. We plot the measured distinguishability of various state pairs in Fig. 4a, and find agreement with these predicted values as well as low distinguishability between eigenstates of odd parity. This distinguishability could be lowered even further by increasing the ratio χ/κ .

The second source of excess dephasing occurs when a pair of qubits switches from an odd parity state to an even parity state. When two qubits coupled to one of the resonators have odd parity, the resonator is resonantly driven by the measurement tone and thus reaches a steady state with a larger number of photons as compared to when the qubits have even parity. If one of these qubits undergoes a bit-flip while the system is in an odd parity state, the resonator frequency shifts and the system undergoes excess dephasing as the resonator rings down to the steady state for the even subspace. The coherence of the logical state is expected to contract

by a factor of $e^{-\bar{n}}$, with \bar{n} being the steady state photon number of a resonator when its qubits are in an odd parity state. From the steady state dephasing rates and the resonator parameters, we independently estimate the photon number in each resonator to be .7 and .6 respectively when the qubits are in the odd state. To measure this effect, we prepare a 3-qubit logical encoding of an X -eigenstate, $|+X_{L'}\rangle = \frac{1}{\sqrt{2}}(|0_{L'}\rangle + |1_{L'}\rangle)$, where L' is one of the four possible logical encodings. With the measurement tone on, but without feedback, we apply a pulse on one (or none) of the qubits, taking the state to a different (or the same) codespace, L . We then tomographically reconstruct the magnitude of the coherence in the new codespace, $|\rho_{01}^L|$, as shown in Fig. 4b. The coherences are normalized to the $|\rho_{01}^L|$ generated by same experiment with the measurement tones off. The system demonstrates significantly less coherence when one of the parities changes from odd to even than vice versa, with reasonable agreement to the expected dephasing based on measured photon number. Since \bar{n} scales inversely with κ for a fixed measurement rate, a larger kappa would reduce this effect.

The third source of excess dephasing is related to static ZZ interactions among the qubits and the uncertainty in timing between when a bit-flip error occurs and when the correction pulse is applied. Performing a Ramsey sequence on Q_i while Q_j is either in the ground or excited state, we measure the coefficients of the system's intrinsic ZZ Hamiltonian, $H_{ZZ} = \frac{1}{2} \sum_{i \neq j} \beta_{ij} Z_i Z_j$. Since the three qubits are in a line topology, with the joint readout resonators also acting as couplers, there is significant coupling between Q_0 and Q_1 ($\beta_{01} = 0.49$ MHz) and between Q_1 and Q_2 ($\beta_{12} = 1.05$ MHz) while there is almost no coupling between Q_0 and Q_2 ($\beta_{02} < 2$ kHz). Due to this

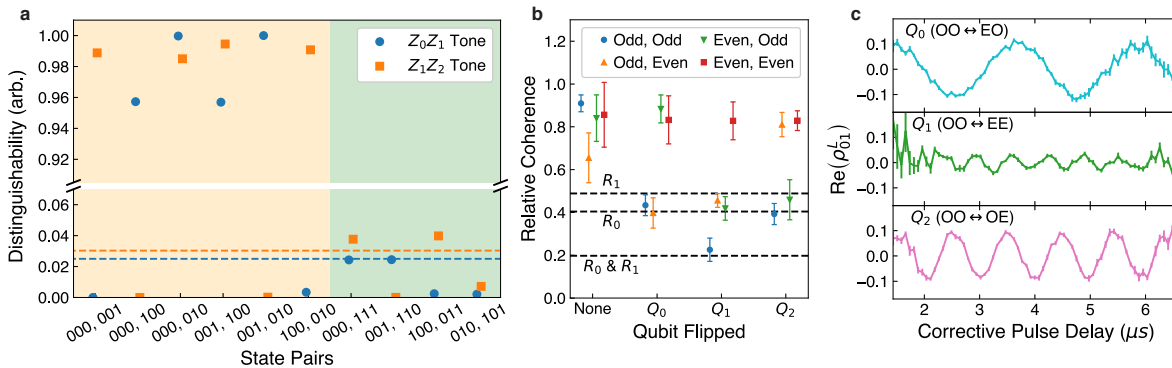


FIG. 4. Preservation of quantum coherence. **a**, Distinguishability of various state pairs in steady state readout for each measurement tone. Pairs of states in the yellow region differ in one or both of their parities. Pairs of states in the green region share their parities. Dashed lines indicate theoretically predicted distinguishability of the even eigenstates. **b**, Relative logical coherence after preparing a logical $|+X_L\rangle$ state in each of the logical parity subspaces, applying parity measurement tones without feedback, and flipping one of the qubits. Coherences are normalized to results from the same procedure without the measurement tones applied. Error bars are statistical uncertainty from repeated runs of the measurement. Dashed lines indicate predicted relative dephasing due to an odd to even parity flip on R_0 , R_1 , or both. **c**, Sample coherences from preparing a logical $|+X_L\rangle$ state in the odd-odd (OO) subspace, applying an error pulse, and letting the controller correct the error. Coherences are reconstructed by time bins set by the time it takes to correct the error with error bars representing statistical uncertainty. Oscillations due to static ZZ coupling are visible.

coupling, the definite parity subspaces have different energy splittings: In the rotating frame of the qubits, the odd-odd, odd-even, even-odd, and even-even subspaces have logical energy splittings of 0 , β_{12} , β_{01} , and $\beta_{01} + \beta_{12}$ respectively. When a bit-flip occurs, the system jumps to an error space and precesses at the frequency of that error space until being corrected by the controller. Since the time from the error flip to the correction pulse is generally unknown, the state can be considered to have picked up a random unknown relative phase. The net dephasing ζ_{zz} can be calculated by averaging the potential phases over the probability distribution of time, T , it takes to correct an error: $e^{i\phi - \zeta_{zz}} = \langle e^{iT\Delta\beta} \rangle_T$ with $\Delta\beta$ being the energy difference between codespace and error space. Using the distributions in Fig. 3a and known $\Delta\beta$, we compute ζ_{zz} to be from 2.5 to 5.7 depending on the codespace and the qubit flipped. Although we don't observe this dephasing directly, we perform an experiment to capture this effect. For each of the codespaces, we prepare a $|+X_L\rangle$ state in the odd-odd codespace and induce a bit-flip error while the feedback controller is active. After $6\ \mu\text{s}$, we perform tomography on all three qubits and note the time at which the correction pulse occurred. We then reconstruct the logical coherence element ρ_{01}^L of the density matrix conditional on time it took the controller to apply the correction pulse. As shown in Fig. 4c, we observe oscillations with frequency corresponding to the effects of ZZ coupling. This source of dephasing is not intrinsic to the protocol, and can be mitigated by reducing the ZZ coupling between the qubits.

Our experiment extends the capabilities of continuous measurements, demonstrating active feedback on multi-

ple multipartite measurement operators. We use continuous quantum error correction to detect bit flips and extend the relaxation time of a logical state. Furthermore, the protocol is implemented in a planar geometry and compatible with existing superconducting qubit architectures so can in principle be combined with other error correction methods. Future improvements could be made by reducing spurious decoherence effects through novel implementations of continuous parity measurements[38, 39] or optimizing coupling parameters. Specifically, increasing χ/κ and increasing κ will reduce dephasing for a given measurement rate. Furthermore, lowering the static ZZ coupling[40] will reduce the observed dephasing from an error occurring at an indeterminate time. Additional feedback could be used to reduce the effects of measurement induced dephasing[41]. By incorporating more qubits and continuous XX measurements, this scheme could be extended to stabilize fully protected logical states[35].

Acknowledgements We thank A. Korotkov, J. Atalaya, R. Mohseninia, and L. Martin for discussions. We also thank J.M. Kreikebaum and T. Chistolini for technical assistance. This material is based upon work supported in part by the U.S. Army Research Laboratory and the U.S. Army Research Office under contract/grant number W911NF-17-S-0008. JD also acknowledges support from the National Science Foundation - U.S.-Israel Binational Science Foundation Grant No. 735/18.

Author contributions E.F., M.S.B., and W.P.L. conceived the experiment. W.P.L. and E.F. designed the chip. W.P.L. fabricated the chip, constructed the experimental setup, performed measurements, and analysed data with assistance from M.S.B. J.D. and A.N.J. provided theoretical support. W.P.L. wrote the manuscript with feedback from all authors. All work was carried out under the supervision of I.S.

Competing interests The authors declare that they have no competing financial interests.

METHODS

Design and fabrication The microwave properties of the chip were simulated in Ansys high-frequency electromagnetic-field simulator (HFSS), and dispersive couplings were simulated using the energy participation method with the python package pyEPR[42]. Resonators, transmission lines, and qubit capacitors were defined by reactive ion etching of 200 nm of sputtered niobium on a silicon wafer. Al-AlO_x-Al Josephson junctions were added using the bridge-free “Manhattan style” method[43]. The junctions were then galvanically connected to the capacitor paddles through a bandaid process[44]. The middle qubit is fixed frequency, and the outer two qubits are tunable with a tuning range of 260 MHz and 220 MHz. Wire bonds join ground planes across the resonators and bus lines.

Measurement setup A wiring diagram of our experimental setup is show in Supplementary Information Figure 1. The Josephson Parametric Amplifiers (JPAs) are fabricated with a single step using Dolan bridge Josephson junctions. They are flux pumped at twice their resonance frequency, providing narrow-band, phase-sensitive amplification. The signals are further amplified by two cryogenic HEMT amplifiers, model LNF4.8. In the output chain for resonator 0, we include a TWPA between the JPA and the HEMT to operate that JPA at a lower gain. Infrared filters on input lines are made with an Eccosorb dielectric. The outer qubits are flux tuned with off-chip coils. The FPGA board provides full control of the qubits and readout of the resonators. An external arbitrary waveform generator creates the cavity tones and JPA drives, as well as triggering the FGPA. The JPA modulation tone is split with one branch phase shifted before both go into an IQ mixer for single sideband modulation.

FPGA Logic The FPGA board we used for the feedback is an Innovative Integration X6-1000M board. We programmed a custom pulse generation core to drive qubit pulses and to demodulate and filter incoming readout signals. A control unit parses instructions loaded in an instruction register. These instructions may include 1) putting a specified number of pulse commands into a queue to await pulse timing; 2) resetting a pulse timer keeping track of time within a sequence while incrementing a trigger counter; and 3) resetting the pulse timer, the trigger counter, and the instruction pointer. When a pulse instruction enters the timing queue, it waits until a specified time and is then sent to one of three different possible locations. The first possible location is a pulse library where the instruction points to a complex pulse envelope of a given duration, which is then modulated by one of three CORDIC sine/cosine generators and sent to the correct DAC. These pulses are sent down one of three qubit control lines. The second possible location is to one of the CORDIC sine/cosine generators, where the instruction will increment the phase of the generator by a specified argument, thus implementing Z rotations

in the qubit frame. The third location is a demodulation core, which, similarly to the qubit pulse block, retrieves a complex waveform from memory for a specified duration. This waveform is then multiplied against the complex incoming readout signals and low-pass filtered with a 32 ns exponential filter to generate the signal V_i^{DC} for feedback as well as to readout projective measurements.

When the feedback control unit is active, it takes V_i^{DC} , applies a secondary 1536 ns ns exponential filter/accumulator to further reduce the noise, and then continuously checks these traces (V_i) against the threshold conditions for an error to have been detected. When an error is detected, the controller injects instructions for a corrective π -pulse into the pulse generation unit. Any voltage V_i which went across a threshold is then inverted as to not trip further corrective pulses. After a delay such that the corrective pulse has taken effect on chip, the V_i^{DC} is inverted before being accumulated into V_i . In conjunction with the previous inversion of V_i , this effectively resets the feedback controller while avoiding interpreting the corrective pulse as another error.

The board’s I/O comprises the PCIe slot for exchanging data with the computer and the ADC/DACs on the analog front-end. The FPGA can stream from multiple sources to the computer along 4 data pipelines. The primary sources are V_i^{DC} and a list of timestamped pulse commands. The timing of any corrective pulses can be obtained from this second source. Further data sources include raw ADC voltages, raw DAC voltages, and V_i , which are only used as diagnostics. On the analog front-end, there are two ADCs running at 1 GSa/s which take in the IF readout signals from the I and Q ports of an IQ mixer, treating the two ADC inputs as the real and imaginary parts of a complex signal. To drive the three qubit lines, there is one DAC running at 1 GSa/s and, due to board constraints, two DACs running at 500 MSa/s.

Optimizing Filter Parameters To optimize threshold values, we prepare the ground state and then flip either one or none of the qubits while taking parity traces (V_i^{DC}). In post processing, we filter the traces with the same exponential filter as on the FPGA to recreate V_i , and classify the resultant traces according to whether or not they pass the different thresholds registering as a qubit flip. We thus get a confusion matrix $P_{ij} = P(i|j)$, the probability of classifying a trace as a flip on i given a preparation flip j , where $i, j \in (\text{None}, 0, 1, 2)$. The thresholds were chosen to minimize $\sum_{ij} (P_{ij} - \delta_{ij})^2$.

- [38] B. Royer, S. Puri, and A. Blais, *4* (2018), [10.1126/sciadv.aau1695](https://doi.org/10.1126/sciadv.aau1695).
- [39] D. P. DiVincenzo and F. Solgun, *New Journal of Physics* **15**, 075001 (2013).
- [40] A. Kandala, K. X. Wei, S. Srinivasan, E. Magesan, S. Carnevale, G. A. Keefe, D. Klaus, O. Dial, and D. C. McKay, “Demonstration of a high-fidelity cnot for fixed-frequency transmons with engineered zz suppression,” (2020), [arXiv:arXiv:2011.07050 \[quant-ph\]](https://arxiv.org/abs/2011.07050).
- [41] A. Frisk Kockum, L. Tornberg, and G. Johansson, *Phys. Rev. A* **85**, 052318 (2012).
- [42] Z. K. Mineev, Z. Leghtas, S. O. Mundhada, L. Christakis, I. M. Pop, and M. H. Devoret, “Energy-participation quantization of josephson circuits,” (2020), [arXiv:2010.00620 \[quant-ph\]](https://arxiv.org/abs/2010.00620).
- [43] A. Potts, G. J. Parker, J. J. Baumberg, and P. A. J. de Groot, *IEE Proceedings - Science, Measurement and Technology* **148**, 225 (2001).
- [44] A. Dunsworth, A. Megrant, C. Quintana, Z. Chen, R. Barends, B. Burkett, B. Foxen, Y. Chen, B. Chiaro, A. Fowler, R. Graff, E. Jeffrey, J. Kelly, E. Lucero, J. Y. Mutus, M. Neeley, C. Neill, P. Roushan, D. Sank, A. Vainsencher, J. Wenner, T. C. White, and J. M. Martinis, *Applied Physics Letters* **111**, 022601 (2017).
- [45] J. Gambetta, A. Blais, M. Boissonneault, A. A. Houck, D. I. Schuster, and S. M. Girvin, *Phys. Rev. A* **77**, 012112 (2008).

SUPPLEMENTARY MATERIALS

A. System parameters

We summarize qubit and resonator frequencies, as well as typical qubit lifetimes in the tables below.

	Q_0	Q_1	Q_2
Frequency (MHz)	5355	5182	5392
Anharmonicity (MHz)	307	310	310
T_1 (μ s)	22	23	23
T_2^* (μ s)	18	26	20
T_2^{echo} (μ s)	31	31	35

TABLE I: Qubit parameters

	R_0	R_1
Frequency (MHz)	6314	6405
κ (kHz)	636	810
χ (MHz)	2.02	2.34
Quantum Efficiency	0.62	0.56

TABLE II: Resonator parameters

B. Tomographic reconstruction

We use the parity resonators to perform qubit tomography. However, due to the nature of the parity condition, not all states are distinguishable by this measurement. To perform tomography, we use single qubit pulses to map each three-qubit Pauli eigenstate to $|000\rangle$ and then measure both resonators on their respective $|00\rangle$ resonance. We then measure the probability that full qubit system is in the ground state, which corresponds to reading out both resonators as 0. We additionally include data into the tomography analysis if one of the resonators reads out 1 and the other reads out 0, since we know the final state to be in either $|100\rangle$ or $|001\rangle$ depending on which resonator reads 1. Using this information, we construct partial Pauli expectation values such

as $\langle X^+Y^-I \rangle$, with P^+, P^- being the plus and minus projectors for a particular Pauli P such that $P = P^+ - P^-$. We then apply readout correction on these probabilities to mitigate the effects of readout infidelity. From this corrected data taken over many tomographic sequences, we can reconstruct full Pauli expectation values such as $\langle XYI \rangle$. When reconstructing logical coherences, we only measure in the X and Y bases. When reconstructing populations, we only measure in the Z basis.

C. Ramsey heralding

Qubits 0 and 2 demonstrate a strong temporal bistability in qubit frequency, with a splitting of about 80 kHz and a typical switching time on the order of .1–10 s. When taking data to reconstruct logical coherences, we include five extra sequences in our AWG sequence table, each consisting of five repeated restless Ramsey measurements with free precession times of 6 μ s. With a typical initial sequence length of 64 and a repetition rate of 100 μ s, the qubit’s frequency state is sampled every 7 ms, allowing us to herald data runs to only include data from runs when the qubits have a particular frequency.

D. Steady state dephasing

Here we derive relative dephasing rates for two qubits in a dispersive parity measurement using a classical analysis of the resonator steady states. The measurement dephasing rate is proportional to the distinguishability of resonator responses when the coupled qubits are in different eigenstates[45]. We set the probe frequency on resonance with the cavity when qubits are in the single-excitation subspace and assume that $\chi \gg \kappa$. We also assume the external cavity coupling is much larger than the internal cavity loss, so the cavity responds with the following scattering parameter:

$$S(f_0 := \chi \langle Z_0 + Z_1 \rangle) = \frac{-2f_0 + i\kappa}{-2f_0 - i\kappa} \quad (\text{S.1})$$

Odd parity states are perfectly indistinguishable. The distinguishability between states of opposite parity is

$$D_{01,00} = |S(0) - S(2\chi)|^2 = \left| (-1) - \frac{-4\chi + i\kappa}{-4\chi - i\kappa} \right|^2 \approx 4 \quad (\text{S.2})$$

With $z \equiv 4\chi + i\kappa$, the distinguishability between the two even parity states is:

$$\begin{aligned} D_{11,00} &= |S(-2\chi) - S(2\chi)|^2 = \left| \frac{4\chi + i\kappa}{4\chi - i\kappa} - \frac{-4\chi + i\kappa}{-4\chi - i\kappa} \right|^2 \\ &= \left| \frac{z}{\bar{z}} - \frac{\bar{z}}{z} \right|^2 = \left| \frac{z^2 - \bar{z}^2}{|z|^2} \right|^2 = \left| \frac{(z + \bar{z})(z - \bar{z})}{|z|^2} \right|^2 \\ &= \left(\frac{(8\chi)(2\kappa)}{16\chi^2 + \kappa^2} \right)^2 \approx \left(\frac{\kappa}{\chi} \right)^2 \end{aligned} \quad (\text{S.3})$$

From these equations, we get the following relative dephasing (Γ) and measurement rates (Γ^m) between states of different parity and states of even parity:

$$\frac{\Gamma_{01,00}}{\Gamma_{11,00}} = \frac{\Gamma_{01,00}^m}{\Gamma_{11,00}^m} \approx \frac{4\chi^2}{\kappa^2} \quad (\text{S.4})$$

E. Dynamic Dephasing

When the resonator is not at steady state, one can have significantly increased dephasing rates after a parity flip. Here we will consider the effect of a bit flip error taking an odd parity qubit state to an even parity state while the parity measurement is on. In this case, the measurement tone is on resonance with the cavity and the cavity field will initially be in a steady state α_0 . When the qubit parity is flipped from odd to even, the cavity evolves as two copies, one for each even parity basis state (α_{00} and α_{11}). As a simplifying approximation, we assume the measurement tone is turned off at the moment the parity changes as to capture just the transient dynamics. There are two equivalent methods[45] to calculate the net dephasing ζ . The first can be obtained by integrating the rate at which information leaves the cavity, $\Gamma_\phi^m = \frac{\kappa}{2} |\alpha_{00} - \alpha_{11}|^2$. The second can be obtained by integrating the rate at which the cavity dephases the qubit, $\Gamma_\phi = 4\chi \text{Im}[\alpha_{00}\alpha_{11}^*]$, with 4χ being the frequency difference between the $|00\rangle$ resonance and the $|11\rangle$ resonance. Here we use the second method to simplify the calculation. We work in the rotating frame of the odd-parity resonance and define $k \equiv \kappa/2 - 2i\chi$ to get two cavity equations, one associated with each basis state:

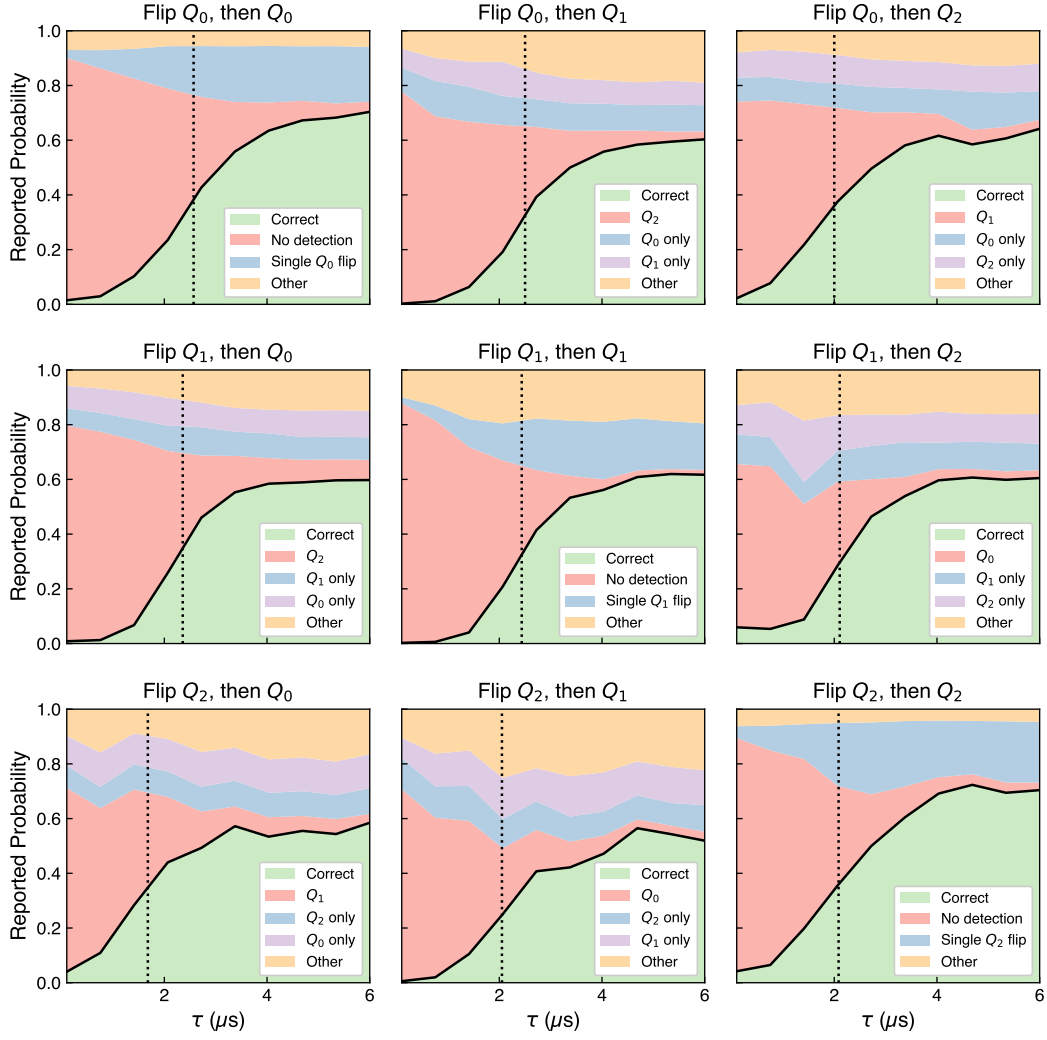
$$\begin{aligned} \dot{\alpha}_{00} &= \left(2\chi i - \frac{\kappa}{2} \right) \alpha_{00} \\ \dot{\alpha}_{11} &= \left(-2\chi i - \frac{\kappa}{2} \right) \alpha_{11} \end{aligned} \quad (\text{S.5})$$

$$\begin{aligned} \alpha_{00}(t) &= \alpha_0 e^{-kt} \\ \alpha_{11}(t) &= \alpha_0 e^{-\bar{k}t} \end{aligned} \quad (\text{S.6})$$

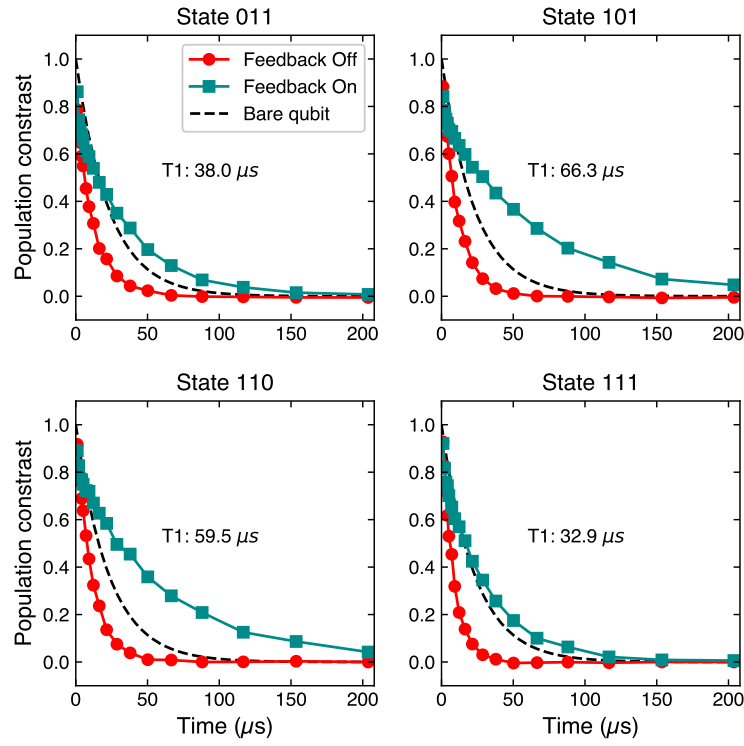
$$\begin{aligned} \zeta &= \int_0^\infty 4\chi \text{Im}[\alpha_{00}\alpha_{11}^*] dt = 4\chi \text{Im} \left[\int_0^\infty \alpha_{00}\alpha_{11}^* dt \right] \\ &= |\alpha_0|^2 4\chi \text{Im} \left[\int_0^\infty e^{-2kt} dt \right] \\ &= |\alpha_0|^2 4\chi \text{Im} \left[\frac{1}{2k} \right] = |\alpha_0|^2 4\chi \text{Im} \left[\frac{2\bar{k}}{|2k|^2} \right] \\ &= |\alpha_0|^2 \frac{16\chi^2}{\kappa^2 + 16\chi^2} \approx |\alpha_0|^2 \end{aligned} \quad (\text{S.7})$$

Therefore, the magnitude of the final coherence between $|00\rangle$ and $|11\rangle$, $|\rho_{00,11}^f|$, will be dephased from the initial coherence between $|01\rangle$ and $|10\rangle$, $|\rho_{01,10}^i|$:

$$\left| \rho_{00,11}^f \right| = e^{-\zeta} \left| \rho_{01,10}^i \right| = e^{-|\alpha_0|^2} \left| \rho_{01,10}^i \right| \quad (\text{S.8})$$



Extended Data Figure 2. Extended data plot for Fig. 3b. Pairs of qubits are flipped with varying time between flips. When different qubits are flipped, the red region represents the controller detecting a flip on the third qubit, resulting in a logical error. When the same qubit is flipped twice, the red region represents the probability of the controller not detecting a flip (which is not a logical error). Blue and purple regions represent the probability of a single flip being detected. The orange region represents the probability of the controller detecting some other sequence of flips. Dotted lines represent the dead time, when the red probability matches the green probability.



Extended Data Figure 3. Extended data plot for Fig. 3c. Effective T_1 for all four definite parity subspaces are measured and fit to an exponential. Blue traces are taken with feedback off. Orange traces are taken with feedback on. The black dotted line represents the lifetime of a bare qubit (24 μs).